





## Room-temperature coherence boosting of molecular graphenoids by environmental spectral decomposition

Federico Lombardi <sup>1,\*</sup>, Ming-Yee Tsang,<sup>1</sup> Michele Segantini <sup>2</sup>, Ji Ma,<sup>3</sup> William K. Myers <sup>4</sup>,  
Xinliang Feng,<sup>3</sup> Boris Naydenov,<sup>2</sup> and Lapo Bogani <sup>1,†</sup>

<sup>1</sup>*Department of Materials, University of Oxford, 16 Parks Road, Oxford OX1 3PH, United Kingdom*

<sup>2</sup>*Institute for Nanospectroscopy, Helmholtz-Zentrum Berlin für Materialien und Energie GmbH, 14109 Berlin, Germany*

<sup>3</sup>*Centre for Advanced Electronics, Faculty of Chemistry and Food Chemistry, Technische Universität, Mommsenstraße 4, 01069 Dresden, Germany*

<sup>4</sup>*Inorganic Chemistry, University of Oxford, South Parks Road, Oxford OX1 3QR, United Kingdom*



(Received 29 July 2021; accepted 23 February 2022; published 9 March 2022)

We explore the usage of pulse sequence optimization to boost the quantum properties of topological defects in molecular graphenoids at high temperatures. We reach spin-lattice relaxation times on the same order as those of the best quantum devices in the literature,  $\sim 1$  ms at room temperature. The coherence time is shown to be heavily affected by the hyperfine interaction and by the high concentration of hydrogen atoms in particular. We test and compare the applicability and performance of different decoupling sequences in enhancing the coherence, identifying the best-performing sequences for the purposes of robust state initialization and coherence optimization. Coherence times up to  $30 \mu\text{s}$  are reached, and we provide insight into the system-environment interaction mechanisms, with a semiclassical model that considers the nuclear bath as a source of a classical random noise and the dynamical decoupling as a filter function. Full deconvolution of the noise spectrum of the bath is obtained, and we show the noise density has a Lorentzian shape whose parameters describe the nuclear-bath dynamics.

DOI: [10.1103/PhysRevB.105.094106](https://doi.org/10.1103/PhysRevB.105.094106)

### I. INTRODUCTION

The key concept of solid-state quantum information devices is that of a spin coupled to a noisy environment that causes decoherence [1]. The necessity of reducing this noise, and consequently extending the coherence time, is at the heart of the use of cryogenics in quantum systems. The study of the noise and its dephasing effects is thus especially important for high-temperature quantum systems and lies at the heart of raising the operating temperature of quantum devices. By reducing the effective interaction between the spin and its environment, it has been possible to extend the coherence times of defect centers in solid-state systems by several orders of magnitude [2]. Central to these methods are dynamical decoupling techniques, which can minimize the effects of nuclei-induced decoherence [3,4]. Spectral decomposition techniques are a key aspect to unravel the various dynamic components in the solid-state spin bath [5], and they offer a fundamental tool to boost the quantum coherence properties.

Molecular graphenoids are graphene-based systems that allow creating aromatic structures with full control over the edge topology and morphology. They offer an exciting experimental ground to test theoretical predictions about the quantum properties of carbon nanostructures, and they offer

perspective technological advantages for spintronics [6], batteries [7], nonlinear optics [8], and optically induced singlet fission [9]. A large body of theoretical work has studied magnetism in graphene nanoflakes and the possibility of introducing spins through defects or topological alterations [10,11]. As individual units of the graphenoids' honeycomb lattice can be shaped to resemble defects, such as pentagonal or heptagonal rings, they also offer model systems for quantum units based on carbon and display excellent coherence times. There is considerable interest in having delocalized spins in graphenelike nanostructures to be used as quantum systems [12]. Excellent quantum properties were demonstrated in graphene nanoribbons [13] and in graphenoids, up to room temperatures [14].

As a consequence, graphenoids appear to be extremely appealing prospective systems for room-temperature quantum processing. Quantum systems such as donors in Si [15], nitrogen vacancy (NV) centers in diamond [16], and color centers in SiC [17] have undergone several years of optimization and are more established. Graphenoids, on the other hand, do compare favorably to shallow NV centers [18] and nanodiamonds [19] at room temperature. Additionally, their chemistry offers the possibility of functionalization with photo- or bioactive groups, and they already outperform all metal-based molecular systems above 80 K [20–24].

Current limitations to the performance of molecular graphenoids are due to environmental nuclei, which are strongly detrimental to electron spin coherence. There are numerous approaches that can be used to mitigate

\*federico.lombardi@materials.ox.ac.uk

†lapo.bogani@materials.ox.ac.uk

nuclei-induced decoherence: isotopic enrichment, clock transitions, and dynamical decoupling.

The first approach is the most effective [25–28], but it is also very expensive. Moreover, it is not generally applicable because not all elements have nuclear-spin-free isotopes. For example,  $^{13}\text{C}$  and  $^{29}\text{Si}$  can be substituted with  $^{12}\text{C}$  and  $^{28}\text{Si}$ , which do not have nuclear spin, whereas hydrogen can be substituted with deuterium, which has a much lower gyromagnetic ratio but still retains a nuclear spin. Clock transitions are special avoided-crossing points for which the magnetic field becomes insensitive to fluctuations, to first order. In numerous systems, working around clock transitions has resulted in strong increases in coherence [29–32]. Nevertheless, clock transitions are not present in all complexes and are usually related to systems with strong hyperfine couplings or zero-field splittings typical of heavier elements.

Instead of relying on engineering the quantum system itself, dynamical decoupling relies on the engineering of the control sequences. In this work, we unravel how the performance of nanosized carbon units, and thus the spin quantum coherence of pentagonal defects in the honeycomb carbon lattice, can be optimized. We show how the coherence times can be boosted up to 0.1 ms at 200 K and 0.03 ms at room temperature. In the presence of an environment dominated by interactions with hydrogen nuclei, we model the bath as a classical noise, and we achieve the deconvolution of its spectral density.

## II. THE SYSTEM

### A. Graphenoid system and its decoherence

The molecular graphenoid under study is shown in Fig. 1. The presence of two pentagonal sites included in the hexagonal lattice introduces an imbalance in the sublattices. According to Lieb's theorem [33], such an imbalance gives rise to a system with  $S = 1$ , and the molecule is a singlet ground state with a closely lying, thermally accessible triplet excited state, which becomes populated at higher temperature  $T$ . We describe the Hamiltonian as a central electron-spin system coupled to a nuclear bath (in units of  $\hbar$ ):

$$\hat{H} = \hat{H}_S + \hat{H}_{SB} + \hat{H}_B \quad (1)$$

$$= \hat{S}J\hat{S} + \mu_B g B \hat{S}_z + \hat{\mathbf{S}}\hat{\mathbf{D}} + \sum_{i=1}^N \hat{\mathbf{S}}\mathbf{A}_i\hat{\mathbf{I}}_i + \sum_{i=1}^N \mu_n g_n B \hat{I}_z + \sum_{i \neq j}^N \hat{\mathbf{I}}_i \mathbf{P}_{ij} \hat{\mathbf{I}}_j, \quad (2)$$

where  $\hat{\mathbf{S}}$  and  $\hat{\mathbf{I}}$  are electron- and nuclear-spin operators, respectively;  $J$  is the exchange coupling;  $\mathbf{B}$  is the external magnetic field;  $\mu_B$  is the Bohr magneton;  $g$  is the Landé factor;  $\mathbf{D}$  is the zero-field splitting tensor;  $\mathbf{A}_i$  are the hyperfine-coupling tensors;  $N$  includes all nuclei coupled to the central spin (the 68 H in the molecule plus any other spin-active nucleus in the matrix within a limited radius in the vicinity of the molecule);  $\mu_n$  is the nuclear magneton;  $g_n$  is the isotropic nuclear Landé factor; and  $\mathbf{P}$  includes all types of nuclear-nuclear interactions.

The first three terms of the Hamiltonian exclusively describe the electron-spin system: from previous measurements [14], we know that  $J = 550$  K,  $g = 2.0027$  (which we can consider largely isotropic) and that the largest principal value

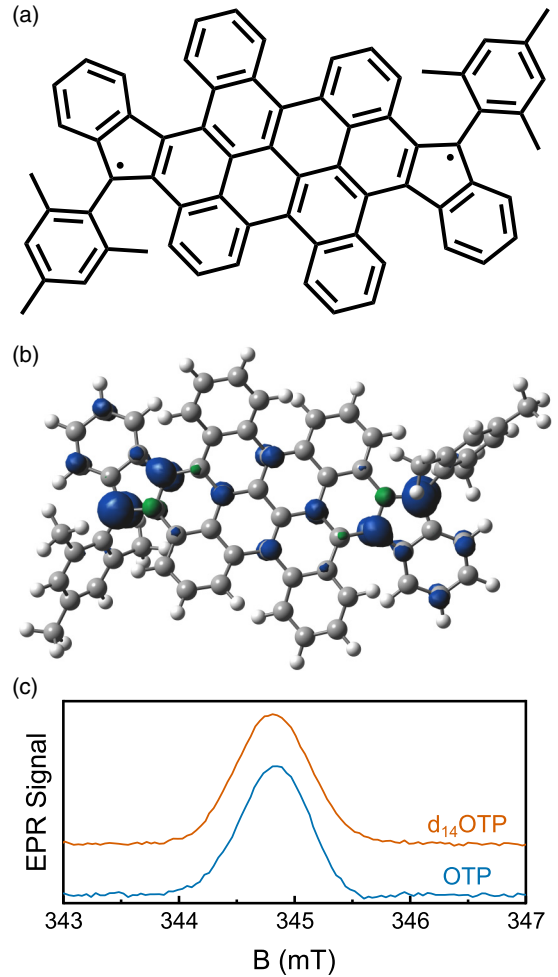


FIG. 1. (a) Chemical scheme of the molecule under study. (b) Three-dimensional structure of the molecule under study (gray = C, white = H) and spin density calculated by DFT using the Becke, 3-parameter, Lee-Yang-Parr functional (B3LYP) with the 6-31G\*\* basis set, with an isovalue of 0.005. (c) Echo-detected field sweep at room temperature in OTP and  $d_{14}\text{OTP}$  (9.7 GHz); the two spectra are arbitrarily stacked vertically for clarity.

of  $\mathbf{D}$  is limited as  $D < 1\text{MHz}$  (which is common for largely delocalized spins in organic molecules [34–36]). The hyperfine term incorporates the system-bath interaction. Hyperfine coupling is not resolved in Fig. 1(c) and contributes only to increasing the width of the spectrum, indicating weakly coupled hydrogen nuclei. The latter two terms in Eq. (1) refer purely to the nuclear bath: they have a negligible effect on the field-sweep spectrum but strongly contribute to the spin dynamics. In particular, we can simplify  $\mathbf{P}_{ij}$  to represent only nuclear-nuclear dipolar interactions. If we consider only the secular term of the dipolar interactions, we can write it with the point-dipole approximation:

$$P_{ij} = \frac{\mu_0 \gamma_i \gamma_j \hbar^2}{4\pi R_{ij}^3} (1 - 3 \cos^2 \theta), \quad (3)$$

where  $\gamma_i$  and  $\gamma_j$  are the gyromagnetic ratios of the  $i$ th and  $j$ th nuclei,  $R_{ij}$  is the distance between the two nuclei, and  $\theta$  is the angle between the distance vector and  $\mathbf{B}$ . At the experimental

$\mathbf{B} = 333$  mT the Larmor frequencies of the electron spin and the hydrogen nucleus are  $\omega_S = 9.3$  GHz and  $\omega_n = 14.2$  MHz, respectively. Therefore, we can establish the following hierarchy for the Hamiltonian contributions:  $J \gg \omega_S \gg \omega_n > A > D \gg P$ .

The description of decoherence can start from considering an arbitrary superposition of states:

$$|\psi(t=0)\rangle = \cos\frac{\theta}{2}|\uparrow\rangle + e^{i\phi}\sin\frac{\theta}{2}|\downarrow\rangle, \quad (4)$$

where  $|\uparrow\rangle$  and  $|\downarrow\rangle$  refer to  $m_s = 0$  and  $m_s = \pm 1$  of the spin Hamiltonian, the angle  $\theta$  describes an initial condition, and  $\phi$  represents a phase difference between the two states. In our experiments the superposition of states is generated by the first pulse; therefore,  $\theta = \pi/2$ .

Two parameters are used to describe the quantum properties of the molecular graphenoid: the spin-lattice relaxation time  $T_1$  and the coherence time  $T_2$ .  $T_1$  characterizes the time constant for a spin flip, which requires an exchange of energy that needs to be provided or absorbed by the lattice.  $T_2$  is usually referred to as the survival of a coherent superposition of states of an individual quantum system. Since our measurements are on ensembles,  $T_2$  is not rigorously defined, and we define  $T_m$  as the coherence time [37], including in it the instantaneous diffusion and partial dilution of the randomly oriented ensemble, so that  $T_m \leq T_2$ . Theory shows that the maximum limit to coherence is given by the spin-lattice relaxation time  $T_2 \leq 2T_1$ . Nonetheless, in multiple practical situations,  $T_1 \gg T_2$ , and the decoherence regime is defined as pure dephasing, in which case the coupling from the environment leads to accumulation of a random phase between the two states:

$$|\psi(t)\rangle = \cos\frac{\theta}{2}|\uparrow\rangle + e^{i\tilde{\phi}(t)}\sin\frac{\theta}{2}|\downarrow\rangle. \quad (5)$$

If we introduce a density-matrix formalism  $\rho = |\psi\rangle\langle\psi|$ , we can quantify and monitor decoherence at any time  $t$  as the ratio between the off-diagonal matrix elements at time  $t$  and at time 0 [5]:

$$W(t) = \frac{|\langle\rho_{\downarrow\uparrow}(t)\rangle|}{|\langle\rho_{\downarrow\uparrow}(0)\rangle|}. \quad (6)$$

Experiments show that  $W(t)$  decays exponentially with a characteristic time  $T_m$ , although this decay might not be strictly a single exponential. We can simplify the system Hamiltonian according to the hierarchy defined above. The large exchange coupling  $J$  places the system in the high-exchange regime: having separated singlet and triplet states does not play a role in the experiment since no transitions can be driven. Hence, this term can be excluded. Additionally, at the  $\mathbf{B}$  used, the Zeeman term dominates the dipolar one by several orders of magnitude, and the spin can be considered quantized on the  $\mathbf{B}$  axis. The system Hamiltonian can thus be simplified:

$$\hat{H}_S = \Omega\hat{S}_z, \quad (7)$$

where we consider the experiment in a rotating framework so that  $\Omega = \omega_S - \omega_{MW}$ , which is common in magnetic resonance [37].

The system-bath and bath Hamiltonians can also be simplified by assuming a pure dephasing regime, i.e.,  $T_1 \gg T_m$  (this hypothesis will be validated by experimental results in Fig. 4

below). Thus, the total Hamiltonian can be written as

$$\hat{H}(t) = [\Omega + \beta(t)]\hat{S}_z, \quad (8)$$

where  $\beta(t)$  is a classical random variable. This semiclassical model describes the effect of the bath as a fluctuating modulation of the resonant frequency of the spin system. It can be related to the Overhauser field produced by the flip flop of neighboring nuclear spins that modify the local  $\mathbf{B}$  perceived by the central spin. Therefore, the quantum origin of this classical noise can be fully mapped onto the intrabath dynamics [38].

Here, we assume  $\beta(t)$  is a Gaussian. Such an assumption relies on the pure dephasing regime and on the fact that the noise is produced by an ensemble of weakly interacting systems, as validated theoretically [39]. Effects arising from non-Gaussian behaviors [40] of  $\beta(t)$  are here disregarded, and we can write

$$\langle\beta(t)\rangle = 0, \quad (9)$$

$$\langle\beta(t)\beta(t+t')\rangle = \xi(t'), \quad (10)$$

where  $\xi$  is the autocorrelation function. The noise spectrum of the nuclear bath is then completely and fully described by the Fourier transform of  $\xi$ :

$$S(\omega) = \int_{-\infty}^{+\infty} \xi(t)e^{-i\omega t} dt, \quad (11)$$

which is the spectral-density function.

## B. Nuclear bath decoupling and filter function

Dynamical decoupling consists of applying a sequence of  $n$  pulses at times  $t_k$  in order to reverse the destructive effect of the environment on quantum coherence [3,41]. The Hahn echo sequence itself can be considered the simplest dynamical-decoupling sequence, as it applies a single refocusing  $\pi$  pulse [42], sufficient to remove any static noise. The Carr-Purcell (CP) sequence increases the number of  $\pi$  pulses to arbitrary  $n$  [43], while the Carr-Purcell-Meiboom-Gill (CPMG) sequence improved CP by modifying the phase of the  $\pi$  pulses in order to be perpendicular to the first pulse [44]. The phase difference between the initial  $\pi/2$  pulse and the decoupling pulses was tuned to remove pulse-formation errors, and CPMG always outperforms CP [4]. The sequences of the XY family (XY4, XY8, XY16) [45,46], which by multi-axis decoupling do not require a stringent phase condition between the first pulse and the train of  $\pi$  pulses, are robust against any initial condition [4].

The above sequences have in common that the interpulse spacing is kept constant (Fig. 2), so they are called periodic dynamical decoupling (PDD). Theoretical understanding of dynamical decoupling led to the development of sequences with unevenly spaced pulses whose positions can be optimized to increase coherence. Analytically constructed sequences, such as Uhrig dynamical decoupling [47], can maximize the performance in a bosonic environment, a result later demonstrated to be universal [48]. Pulse-formation errors arising in PDD can be corrected naturally by concatenated dynamical decoupling, which links together blocks of pulses up to higher orders [49]. An alternative approach to pulsed

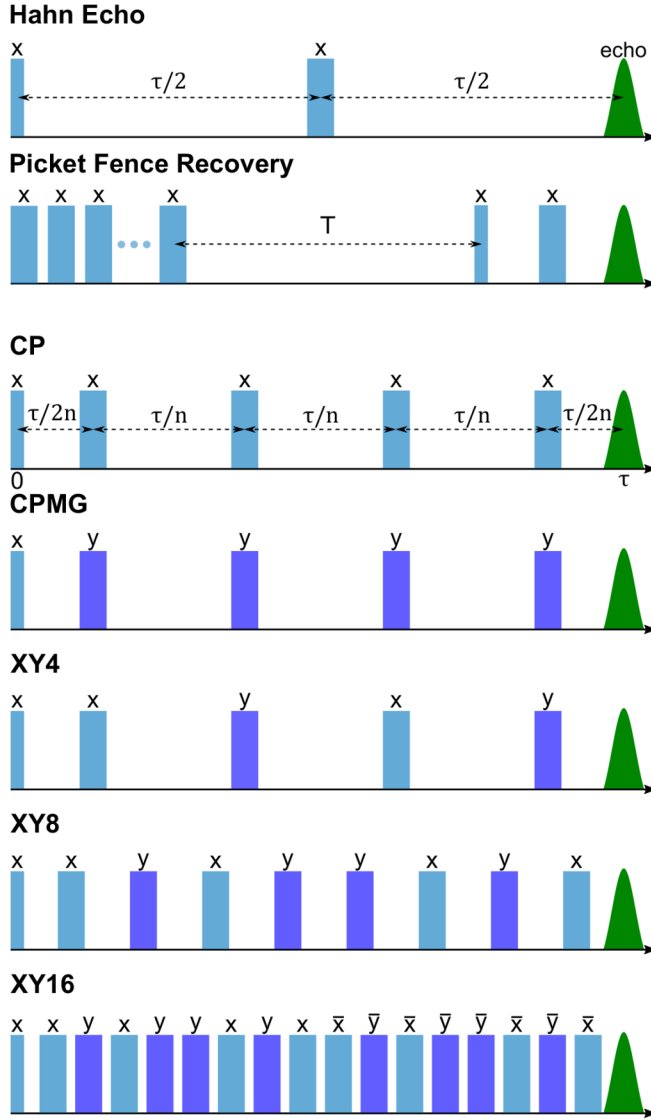


FIG. 2. Pulse sequences used in this paper. In all dynamical-decoupling sequences, the first pulse is a  $\pi/2$  pulse, while the decoupling pulses are  $\pi$  pulses. All sequences are symmetrical. Each  $\pi$  pulse refocuses an echo which is formed at a distance  $\tau$  from the pulse itself, but only the last echo is measured, and its decay is followed while increasing  $\tau$ . Pulses of different phases are in different colors, the letters indicate the phase of the pulse, and the overbars indicate negative phase.

control is continuous dynamical decoupling, in which a continuous drive is used to produce long-lived dressed states [50], which can be combined together with pulsed control [51]. Nonetheless, the complexity added by uneven spacings or by continuous microwave fields is not always matched by a substantial performance increase with respect to PDD [4]. Therefore, most experimental results still rely on the less sophisticated CPMG, which has been employed to impressive results in a plethora of quantum systems, such as NV centers [2,27,52,53], trapped ions [54], and GaAs quantum dots [55].

For a spin system under the general noise spectrum of  $S(\omega)$ , a  $\pi$  pulse in the control sequence flips the sign of the phase accumulation [5,56]. The effect is depicted in Fig. 3

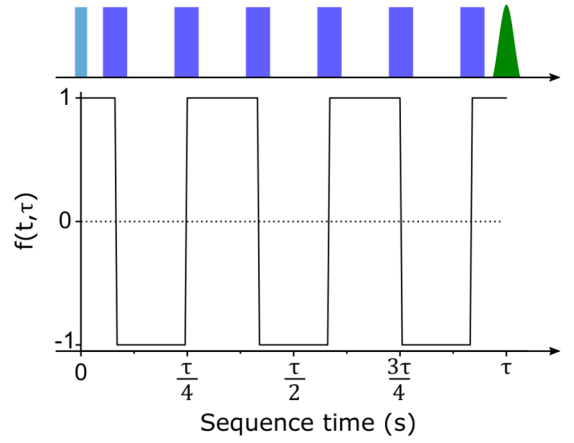


FIG. 3. CPMG6 sequence and trend of the evolution phase. Here, pulses are considered ideal, and the effect of a  $\pi$  pulse is to flip the sign of the evolution.

for CPMG6, assuming ideal pulses (true for  $t_p \ll \tau/n$ ). For  $n$  arbitrary pulses we can then write the evolution of the phase as

$$f(t, \tau) = \sum_{k=0}^{n-1} (-1)^k \Theta(t - t_k) \Theta(t_{k+1} - t), \quad (12)$$

where  $t_0 = 0$ ,  $t_k = \frac{(k-1/2)\tau}{n}$ ,  $t_{n+1} = \tau$ , and  $\Theta(t)$  is the Heaviside step function (see Fig. 3 for this function for CPMG6). The Fourier transform of Eq. (12)  $\tilde{f}(\tau, \omega)$  is the resulting filter function produced by the CPMG sequence. It is equivalent to a high-pass filter, centered at  $\omega_0 = \pi n/\tau$ , with a width of  $\pi/\tau$ . Higher-harmonic components still let high-frequency noise through, but assuming that  $\lim_{\omega \rightarrow \infty} S(\omega) = 0$ , filtering can be improved by decreasing  $\tau$  and increasing  $n$ . The decoherence will then depend on the convolution between the characteristic spectral density  $S(\omega)$  and the  $F(\tau, \omega)$  of the applied control:

$$\chi(\tau) = \frac{1}{2\pi} \int_0^{\infty} S(\omega) |F(\tau, \omega)|^2 d\omega, \quad (13)$$

where  $F(\tau, \omega)$  is the Fourier transform of  $f(t, \tau)$ , so that  $W(\tau) = e^{-\chi(\tau)}$ . From these expressions it is then, in principle, possible to obtain information about the noise spectrum  $S(\omega)$  by measuring the coherence decay of the system and knowing the sequence filter function.

### III. EXPERIMENTAL METHODS

In order to eliminate intermolecular dipolar interactions, we dissolved the graphenoid in *ortho*-terphenyl (OTP) and deuterated OTP ( $d_{14}$ OTP), with a concentration of 1 mM. Samples were transferred to quartz tubes and degassed with five cycles of freeze-pump-thaw to remove oxygen before flame sealing. As the melting temperature of OTP is 329 K, the samples were in the solid state for all the experiments. Measurements were conducted using a Bruker Elexsys E580 electron paramagnetic resonance (EPR) spectrometer equipped with a 1 kW traveling-wave tube amplifier, a dielectric-ring resonator Bruker ER 4118X-MD5, and an Oxford Instruments CF9350 cryostat with an ITC503 controller. For all experiments, the resonator was fully overcoupled to a

$Q$  factor of about 300 to minimize the detection dead time, and the frequency was in the  $X$ -band range, around 9.7 GHz. We used only pulse excitation, with 16 and 32 ns long rectangular  $\pi/2$  and  $\pi$  pulses, respectively.

The experimental apparatus allowed a minimum interpulse distance of 120 ns and a maximum of 31 pulses per sequence. In particular, the limitation here is not only the highest number of pulses but also the minimum interpulse distance, which is quite long because of restrictions on the resonator. Indeed, using a very large number of pulses without being able to reduce the minimum interpulse distance would mean having a long dead time, which makes it much harder to extract relevant time constants.

We measure the spin-lattice relaxation time  $T_1$  using a picket-fence recovery sequence and  $T_m$  with a Hahn echo sequence (see Fig. 2). Several dynamical decoupling sequences were applied, as in Fig. 2, to measure  $T_m^{\text{DD}}$ . In all cases  $\mathbf{B}$  was fixed at the highest value of the echo-detected field sweep seen in Fig. 1(c). The shot-repetition time was always adjusted to be 5 times  $T_1$  so that all spins would be at equilibrium for every new measurement. For all sequences we used an appropriate phase cycling to remove spurious signals.

There are two ways to measure a dynamical decoupling decay with EPR. The first method consists of sending an arbitrarily large number of pulses fixed at a certain interpulse distance and observing the transient echo signal that is refocused by each pulse at half the interpulse distance [see Fig. 5(a) below]. The experiment can then be repeated at different interpulse distances. This is known to produce a modulation in the extracted time constants that reflects the action of nuclei on the central spin [57,58]. The second way keeps the number of pulses fixed, the interpulse distance is incremented, and only the last echo is integrated. The experiment can then be repeated with a varying number of pulses. The two methods employ the same sequence but provide fundamentally different data. The former determines an optimal  $\tau$  value for which the decoupling is at maximum, while the latter describes the behavior of the coherence time while it is regulated by different dynamical decoupling filter functions. Here, we focus on the second approach.

For every measurement we obtain a time trace that we fit with the relevant models using the Levenberg-Marquardt algorithm. We fit the picket-fence recovery data with a double-exponential model,

$$Y(T) = A_1 \exp(-T/T_1) + A_2 \exp(-T/T_{\text{sd}}) + y_0, \quad (14)$$

where  $T_1$  is the spin-lattice relaxation time,  $T_{\text{sd}}$  takes into account the faster spectral diffusion, and  $A_1$  and  $A_2$  are weights for which we always achieve  $|A_1| \gg |A_2|$ , showing that spin-lattice relaxation time dominates the decay. We fit the Hahn echo and dynamical-decoupling data with a stretched exponential model:

$$Y(\tau) = A \exp\left(-\frac{\tau}{T_m}\right)^x, \quad (15)$$

where  $T_m$  is the coherence time and  $x$  is the stretching parameter. In addition to this, when the coherence decay was modulated by nuclear effects, we fit only the peak of each oscillation.

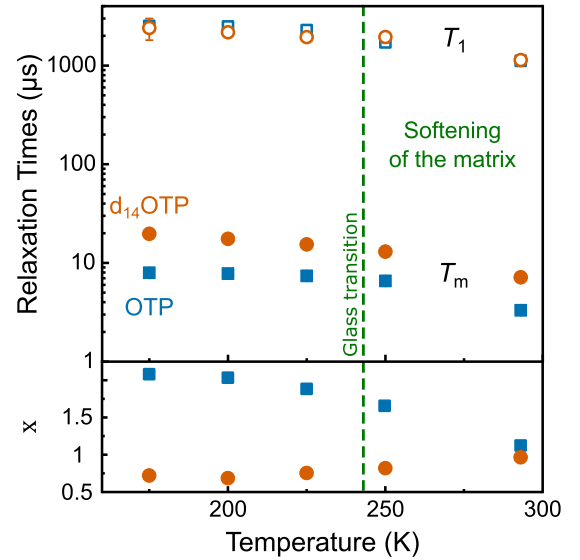


FIG. 4. Temperature dependence of the relaxation times (top) and the stretched parameter  $x$  (bottom). Open symbols show the spin-lattice relaxation time, and solid symbols show the coherence time. Squares show the measurements in OTP, and circles show  $d_{14}\text{OTP}$ . The green dashed line indicates the glass transition temperature (243 K) for OTP and  $d_{14}\text{OTP}$ .

The Hahn echo sequence and the dynamical decoupling techniques represent a direct measurement of the coherence  $W(t)$  as defined in Eq. (6). The main limitations of the measurement are the dead time and the discrete time acquisition, which can distort the theoretical profile of the coherence decay. The function  $Y(\tau)$  in Eq. (15) relates to  $W(t)$  because it provides the phenomenological model to interpret the decay and extract meaningful parameters that can be compared across measurements. Nonetheless, we use the experimental measurements of  $W(t)$  and the theoretical expression of the filter function to deconvolute the integral in Eq. (13) and yield a discrete representation of  $S(\omega)$  as described in Sec. IV C.

## IV. RESULTS AND DISCUSSION

### A. Relaxation times

We first analyze the relaxation behavior while varying the temperature in the 175 to 293 K range. As can be seen from Fig. 4,  $T_1$  monotonically decreases with increasing temperature, and there is negligible difference between the results in the protonated and deuterated matrix since nuclear spins have little impact on spin-phonon interactions. Similarly,  $T_m$  decreases with increasing temperature, with the difference between the two matrices owing to the lower gyromagnetic ratio of deuterium, which produces a weaker nuclear-nuclear dipolar coupling and therefore longer  $T_m$ . The most striking difference between OTP and  $d_{14}\text{OTP}$ , however, is the stretching parameter  $x$ , which can be related to the main decoherence channel. We define the rate of dephasing as a sum of different contributions:

$$\Gamma = \Gamma_{\text{NSD}} + \Gamma_{\text{motion}} + \Gamma_{\text{id}} + \frac{1}{2T_1}, \quad (16)$$

where  $\Gamma_{\text{NSD}}$  refers to nuclear-spin diffusion (NSD),  $\Gamma_{\text{motion}}$  is the contribution of molecular motions, and  $\Gamma_{\text{id}}$  is the contribution of instantaneous diffusion.

From Fig. 4, we see that  $T_1 \gg T_m$ , so we can disregard the latter term at any temperature because of our assumption of pure dephasing. We have checked for instantaneous diffusion at 293 K by measuring  $T_m$  with shorter  $\pi$  pulses in the echo sequence: 6% and 7% increases are reported in OTP and  $d_{14}\text{OTP}$ , respectively, after removing all effects from the  $\pi$  pulse. This increase shows a moderate effect of instantaneous diffusion, but it also indicates that it cannot be responsible for the threefold decrease in  $T_m$  from 200 to 293 K. Therefore, we will disregard the term.

We can divide the first two contributions into matrix-related and system-related components:

$$\begin{aligned}\Gamma &= \Gamma_{\text{NSD}} + \Gamma_{\text{motion}} \\ &= \Gamma_{\text{NSD}}^{\text{m}} + \Gamma_{\text{NSD}}^{\text{s}} + \Gamma_{\text{motion}}^{\text{m}} + \Gamma_{\text{motion}}^{\text{s}},\end{aligned}\quad (17)$$

but for  $\Gamma_{\text{motion}}$  we can disregard matrix effects below the glass temperature. In OTP, the stretch parameter  $x \sim 2$  highlights that the main decoherence channel is NSD. In this case, it is not possible to distinguish between the system and matrix bath because they both contain hydrogens. On the other hand, in  $d_{14}\text{OTP}$  the nuclear bath of the matrix consist of deuterium, which has a gyromagnetic ratio one sixth that of hydrogen. From Eq. (3) we see that for homonuclear dipolar coupling,  $P \propto \gamma^2$ . Therefore, the deuterium bath has much slower dynamics than the hydrogen bath. The EPR literature estimates a decrease of NSD by a factor of 10 to 30 upon deuteration [37,59]. Thus,  $\Gamma_{\text{NSD}}^{\text{s}} \gg \Gamma_{\text{NSD}}^{\text{m}}$ . In the case of  $d_{14}\text{OTP}$ , however,  $\Gamma_{\text{NSD}}^{\text{s}}$  is affected by only the 68 hydrogens in the molecules, producing a bath that is numerically smaller than the one in OTP (system + matrix). Hence, the molecular-motion term  $\Gamma_{\text{motion}}^{\text{m}}$ , which is unmodified in the two matrices, becomes the largest contribution, explaining the value of the stretch parameter of  $\sim 0.6$ .

Above the glass-transition temperature of the matrix, when the matrix enters a viscous regime, self-rotation becomes relevant [60,61], and the matrix physical behavior starts to approach that of an isotropic liquid. As can be seen, OTP and  $d_{14}\text{OTP}$  stretch parameters converge toward the same value because the two matrices are similar, except that  $d_{14}\text{OTP}$  has a larger inertia because deuterium is heavier than hydrogen. The coherence time in  $d_{14}\text{OTP}$  remains larger than that in OTP because the effect of the matrix nuclear spin is no longer negligible. Although current instruments do not allow measurements above 300 K, based on previous comparisons between toluene and deuterated toluene [14], we expect the two matrices to converge to stretch parameter  $x = 1$  and identical  $T_m$  above the melting temperature of 329 K.

## B. Sequence testing

Here, we address, from the perspective of molecular graphenoids, some of the uncertainty in the magnetic-resonance literature about the effects of coherence-enhancing pulse sequences. CPMG sequences on nuclear states show surprisingly long and stretched decays attributed to the non-ideality of  $\pi$  pulses that have a finite length: during the pulse duration, the time-dependent Hamiltonian of the system is

active [62–64]. In EPR, when the bandwidth of the pulses is not sufficient to excite the entire spectrum, a CPMG sequence can lead to a spurious signal that overlaps with the echo [65], which can be partially prevented by advanced cycling of the pulse phases [57,66,67].

The use of CPMG in the molecular graphenoids is substantially different than in many previously discussed systems: the full spectrum is 1.5 mT wide, while the bandwidth of a 16 ns rectangular pulse is 1.33 mT, i.e., enough to excite most of the spectrum [Fig. 1(b)]. The use of 8 ns pulses yielded the same results, as expected. We can compare two-step and  $2^n$ -step phase cyclings, where  $n$  is the number of  $\pi$  pulses in the decoupling train: the former, which phases only the first pulse on the  $\pm x$  channel, is standard CPMG; in the latter all pulses except the last are phased on their  $\pm x$  channel, and we call it CPMG $_{\pm}$ . Analogously, we will call CP $_{\pm}$  the sequence entailing a  $2^n$  phase cycling based on CP. The purpose of CPMG $_{\pm}$  is to cover all possible phase relationships [68].

In Fig. 5(a) we compare the transient echoes of all different phase cyclings in an eight-pulse decoupling sequence with the same interpulse spacing. The decay of the echo intensity at different times indicates that CPMG presents the slowest decay, CP yields the fastest decay, and the two CPMG $_{\pm}$  and CP $_{\pm}$  sequences with 256-step cycling have intermediate performance, with the exact same decay trend but differing by the sign of the echo. It is somewhat expected for a CP sequence to perform worse than CPMG [4] because the longitudinal pulse axis (phase  $y$ ) removes the pulse errors that occur when the pulse axis is transverse with respect to the spin vector (phase  $x$ ). It is very surprising, however, that a more complete phase cycling not only removes the possible spurious signal but also equalizes CP and CPMG. This result thus shows that the  $2^n$ -step phase cycling makes the sequence more robust to the initial condition, but at the cost of lower performance.

Figures 5(b) and 5(c) prove that this difference between the two-step and the  $2^n$ -step phase cyclings is preserved for any number of  $\pi$  pulses  $n$ . Good agreement is obtained between the data and a polynomial dependence on  $n$ :

$$T_m^{\text{DD}}(n) = T_m n^{\beta}, \quad (18)$$

where  $T_m$  is here considered a free parameter and  $\beta$  is an enhancement factor: the larger  $\beta$  is, the better the performance of the sequence is. Whatever  $B$  and frequency (9 and 34 GHz were probed, i.e.,  $X$  and  $Q$  bands) are used, the same enhancement is observed. Even when changing  $T$  to 200 K or switching samples to the  $d_{14}\text{OTP}$  matrix, CPMG always prolongs  $T_m$  more than CPMG $_{\pm}$ . On the other hand, the performance of the CPMG $_{\pm}$  experiment in terms of the  $\beta$  exponent is analogous to the XY sequences. Because CPMG is known to offer better decoupling than XY, but with stronger dependence on the initial conditions [4,69], we conclude that, for a sample with a narrow spectrum that is well excited by a short  $\pi$  pulse, a two-step pulse cycling is sufficient to remove spurious signals, whereas the  $2^n$ -step cycling removes the dependence on the initial condition by mimicking the effect of pulses on both axes at the cost of performance. Additionally, the  $2^n$ -step phase cycling is more costly than the XY sequences that can achieve the same result, but without the complexity of large numbers of cycles. CPMG $_{\pm}$  will thus

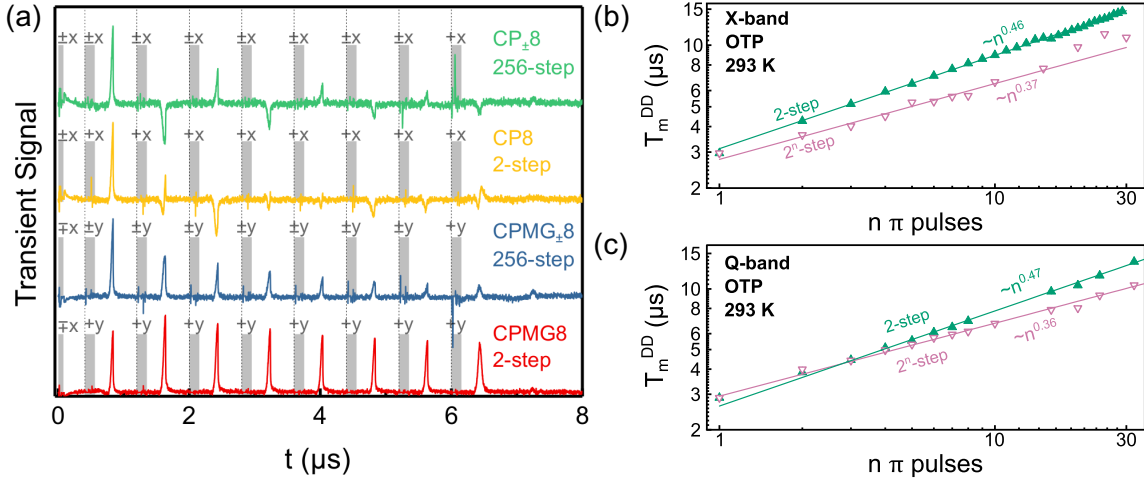


FIG. 5. (a) Transient recording of the signal for CP8 and CPMG8 with two different phase cyclings as described in text. The gray rectangles indicate the pulse position with their phase and the negative or positive channel. (b) Room-temperature X-band (9 GHz) measurements of the coherence time in OTP under CPMG dynamical decoupling. (c) Room-temperature Q-band (34 GHz) measurements of coherence time. Solid lines are fit with the polynomial equation in the text. Solid green triangles are CPMG sequences, while open pink triangles are CPMG $\pm$  sequences.

be considered redundant with respect to XY sequences in the following.

### C. Dynamical decoupling

In Fig. 6 we show the behavior of time decay traces when applying different sequences with their fits, and in Fig. 7 we present the results for all the dynamical decoupling sequences for both matrices at 200 and 293 K, fitting the data with Eq. (18). At every  $T$  and in every matrix, CPMG outperforms other sequences, while XY4, XY8, and XY16 appear roughly equivalent. It appears that up to  $n = 30$  pulses, there is no benefit in switching to XY pulses, probably because the accumulated pulse-formation error is not large enough.

In rationalizing the effect of dynamical decoupling, it has been argued that the enhancement factor from a pulse train is described by  $T_m^{DD} = T_m n^{(1-1/x)}$ , where  $x$  is the stretched parameter of the Hahn echo fit from Eq. (15) [70]. This implies that the enhancement of  $T_m$  can be achieved only when  $x > 1$ , when nuclear-spin diffusion is the dominant factor. Conversely, here, we demonstrate that  $T_m$  always increases

with  $n$ , even for  $x < 1$ , which is the case for the  $d_{14}$ OTP matrix at 200 K.

In NV centers,  $T_m^{DD}$  is enhanced by a factor  $\beta = 2/3$  [52], and an analogous scaling with  $n$  is found in several other systems: spin qubits in GaAs lead to  $\beta = 0.72$  [71], and  $\beta = 0.6$  was observed for a solid-state ensemble of malonic acid radicals [66]. Overall, it appears that most systems where the bath is made of nuclear spins— $^{13}\text{C}$  for NV centers, Ga and As nuclei for GaAs quantum dots, and  $^{13}\text{C}$  and H for malonic acid—display  $\beta \approx 0.6$  to  $0.7$ .

The connection between  $\beta$  and the shape of  $S(\omega)$  remains, however, an open question. It has been shown theoretically [52] that  $\beta = 2/3$  for a Lorentzian spectral-density function:

$$S(\omega) = \frac{\eta\tau_c}{\pi} \frac{1}{1 + (\omega\tau_c)^2}, \quad (19)$$

where  $\eta$  is the average interbath coupling strength and  $\tau_c$  is the bath correlation time related to the flip-flop time. Single NV centers show excellent agreement with this theoretical background because they are affected by a few nearby individual nuclear spins in a process well described by an

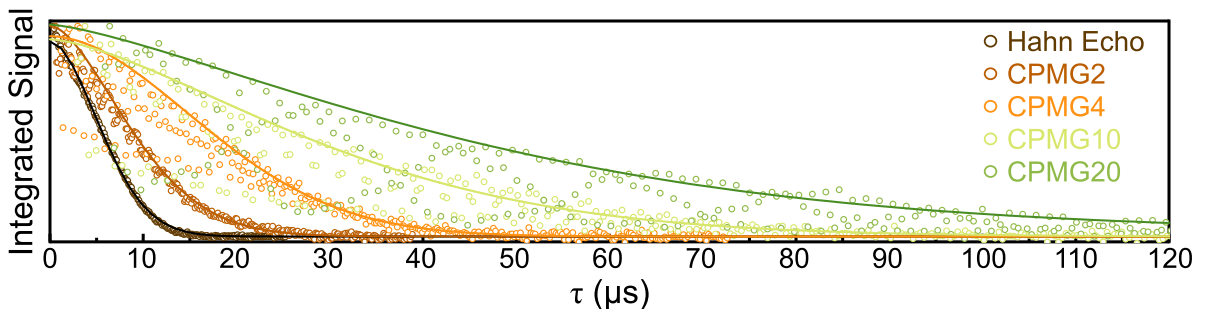


FIG. 6. Coherence decay traces at 200 K for OTP following application of different sequences. It can be observed that a modulation is superimposed on the signal, which is due to the hyperfine coupling to nearby nuclei. Solid lines are fit to the function in Eq. (15). The lines are fit only to the peak of the modulation as discussed in Sec. III.

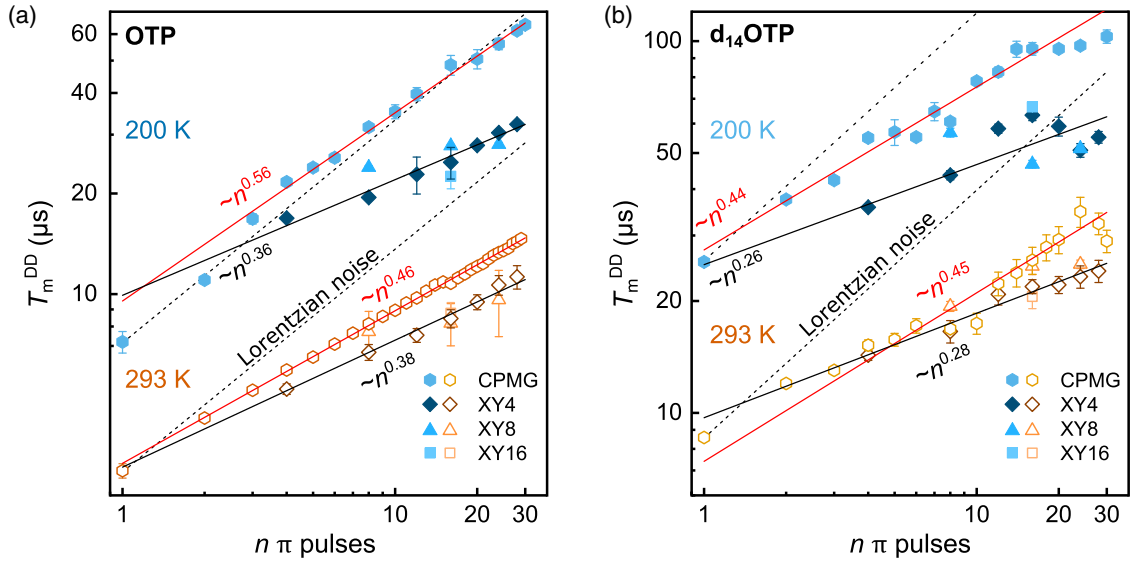


FIG. 7. (a) Summary of coherence time vs number of decoupling pulses at 200 K (solid symbols) and 293 K (open symbols) in OTP. (b) Summary of coherence time vs number of pulses at 200 K (solid dots) and 293 K (open symbols) in  $d_{14}$ OTP. Solid lines are a fit of CPMG data with the polynomial expression in the text. The dashed line is  $T_m^{DD} \sim n^{2/3}$ , which represents the performance under a pure Lorentzian spectral density function as in Eq. (19).

Ornstein-Uhlenbeck model [52,53]. When the central spin is perturbed by an ensemble of many nuclei, the spectral density agrees better with a  $1/f$  noise, and  $S(\omega) \propto \omega^{-\gamma}$  [71]. The high-frequency tails of the two distributions do not differ very much, and to distinguish these two noise environments, it is thus paramount to achieve good experimental sensitivity to the low-frequency components of  $S(\omega)$ .

In Fig. 7, the dashed line represents an ideal trend that assumes  $\beta = 2/3$  and  $S(\omega)$  as in Eq. (19). A comparison with the experimental data reveals that, in all cases except OTP at 200 K, the molecular graphenoid underperforms with respect to a Lorentzian noise and, more generally, also with respect to the quantum systems mentioned above. We interpret this result by considering a breakdown of the decoherence rate (17). Dynamical decoupling is efficient when acting on the  $\Gamma_{\text{NSD}}$  term: when this is the dominant term, the maximum performance is obtained, as in OTP 200 K, which can be related to the Ornstein-Uhlenbeck picture. On the other hand, the sequence is much less efficient when the  $\Gamma_{\text{motion}}$  term dominates, yielding  $\beta \approx 0.44$  to  $0.46$  for different matrices at different  $T$ . Indeed, the main difference from the quantum systems mentioned above is that they are not affected by any kind of internal motion.

Insight into the reasons for this similarity between the sample in OTP at 200 K and the pure Lorentzian noise can be obtained by extracting the spectral deconvolution of the noise-density function  $S(\omega)$  [53]. The integral in Eq. (13) can be decomposed into a sum of discrete terms, and for CPMG with even  $n$ , the filter function is

$$|\tilde{f}(\omega, \tau, n)|^2 = \frac{4}{\omega^2} \sin^2\left(\frac{\omega\tau}{2}\right) \frac{\sin^4\left(\frac{\omega\tau}{4n}\right)}{\cos^2\left(\frac{\omega\tau}{2n}\right)}, \quad (20)$$

which can be used to construct a matrix  $\zeta$  with elements  $\zeta_{ij} = |\tilde{f}(\omega_i, \tau_j, n)|^2$ , where  $n$  is fixed by the sequence used. Equation (13) then leads to the eigenvalue problem  $\chi = \zeta S$ ,

where the solution is attained with a least-squares approach [53]. For each CPMG trace, we used  $\omega_{\text{step}} = 0.1$  MHz, and we binned the values of the extracted  $S(\omega)$  into 100 bins with  $0 < \omega < 400$  MHz, fixed at the center of every bin. In this way it is possible to extract the full spectral density  $S(\omega)$  vs frequency  $\omega$  by averaging the curves extracted for each CPMG sequence, as shown in Fig. 8. The resulting spectral density shows a leveling off at low frequencies, becoming substantially flat below 25 MHz. This behavior thus agrees better with a Lorentzian noise distribution than  $1/f$  pink noise, as shown in Fig. 8. Additionally, it is a better physical representation to assume that  $\lim_{\omega \rightarrow 0} S(\omega)$  goes to a finite value and not to infinity. From the Lorentzian fit we obtain a value for the

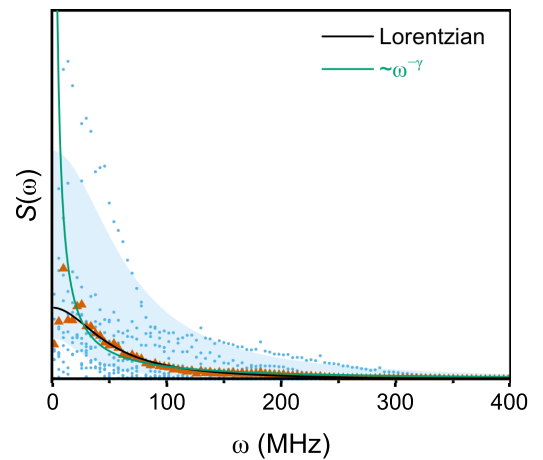


FIG. 8. Spectral density  $S(\omega)$  obtained from the deconvolution of CPMG data in OTP at 200 K. The blue dots are the spectral density function for individual traces, while the orange triangles are their mean. Solid lines are fit with the models discussed in text. The shaded area includes the Lorentzian fitting to the individual CPMG traces.



correlation time from Eq. (19),  $\tau_c = 20 \pm 1$  ns. This value is fully representative of the higher concentration and fast dynamics of hydrogen nuclei in graphenoids and indicates an important source of decoherence. For comparison,  $^{13}\text{C}$  nuclei in NV centers offer values about 500 times slower [53].

## V. CONCLUSIONS

Our results demonstrated how spectral deconvolution and dynamical decoupling techniques can boost the performance of spin-active molecular graphenoids at high temperatures. Some of the uncertainty about the effects of coherence-enhancing pulse sequences was addressed with respect to optimizing the room-temperature behavior of molecular graphenoids, and  $2^n$ -step phase cycling was found to produce more robust results for the initial condition, but at the cost of lower performance overall. For a fixed initial condition, CPMG was revealed to be the best-performing protocol, while the XY family sequences can be employed to allow a more flexible initialization at the cost of lower-level decoupling. These results led to extremely high room-temperature coherence times, up to  $30 \mu\text{s}$ . Moreover, they provided insight into the spectral components of the noise affecting the quantum performance of carbon nanosystems. Noise components in the quantum dynamics of the bath were detected that are linked to nuclear-spin flip flop and molecular motions. The spectral deconvolution provided much deeper insight, not only showing

the shape of the spectral-density function but also revealing a correlation time that is representative of the fast dynamics of hydrogen nuclei. These results validate the use of theoretical frameworks based on the interpretation of nuclear-spin baths as generators of classical Gaussian noise.

Our platform opens the door to exploring the potential advantages of carbon nanostructures at room temperature, including in spintronic devices, where graphene systems have been shown to possess long spin-coherence lengths [72] and outperform metal-based solid qubits [21–24] and shallow-implanted diamond defects [19,73]. Chemical tuning of these graphenoids is now possible, following the indications provided by the analysis of the noise influencing the decoherence. Since the enhancement factor found from CPMG results is affected by molecular motions, which are less susceptible to efficient decoupling, the next natural step would be further engineering, by chemical tuning, of the molecular graphenoids, which would naturally focus on the synthetic tailoring of the edge groups to freeze their motions.

## ACKNOWLEDGMENTS

We thank Dr. D. Alexandropolous for help with sample preparation. This work was financed by the Royal Society (URF and Research Grant), EPSRC (fellowship program Grant No. EP/N509711/1), the European Research Council (ERC-CoG-773048-MMGNRs), and DFG (Grants No. 410866378 and No. 410866565).

- 
- [1] M. A. Nielsen and I. Chuang, *Quantum Computation and Quantum Information* (Cambridge University Press, Cambridge, 2010).
- [2] B. Naydenov, F. Dolde, L. T. Hall, C. Shin, H. Fedder, L. C. L. Hollenberg, F. Jelezko, and J. Wrachtrup, *Phys. Rev. B* **83**, 081201(R) (2011).
- [3] L. Viola, E. Knill, and S. Lloyd, *Phys. Rev. Lett.* **82**, 2417 (1999).
- [4] A. M. Souza, G. A. Álvarez, and D. Suter, *Phys. Rev. Lett.* **106**, 240501 (2011).
- [5] Ł. Cywiński, R. M. Lutchyn, C. P. Nave, and S. Das Sarma, *Phys. Rev. B* **77**, 174509 (2008).
- [6] Y. Morita, S. Suzuki, K. Sato, and T. Takui, *Nat. Chem.* **3**, 197 (2011).
- [7] Y. Morita, S. Nishida, T. Murata, M. Moriguchi, A. Ueda, M. Satoh, K. Arifuku, K. Sato, and T. Takui, *Nat. Mater.* **10**, 947 (2011).
- [8] M. Nakano and B. Champagne, *J. Phys. Chem. Lett.* **6**, 3236 (2015).
- [9] T. Minami and M. Nakano, *J. Phys. Chem. Lett.* **3**, 145 (2012).
- [10] O. V. Yazyev and L. Helm, *Phys. Rev. B* **75**, 125408 (2007).
- [11] O. V. Yazyev and M. I. Katsnelson, *Phys. Rev. Lett.* **100**, 047209 (2008).
- [12] W. Zeng and J. Wu, *Chem* **7**, 358 (2021).
- [13] M. Slota, A. Keerthi, W. Myers, E. Tretyakov, M. Baumgarten, A. Ardavan, H. Sadeghi, C. Lambert, A. Narita, K. Müllen, and L. Bogani, *Nature (London)* **557**, 691 (2018).
- [14] F. Lombardi, A. Lodi, J. Ma, J. Liu, M. Slota, A. Narita, W. K. Myers, K. Müllen, X. Feng, and L. Bogani, *Science* **366**, 1107 (2019).
- [15] R. C. C. Leon, C. H. Yang, J. C. C. Hwang, J. C. Lemyre, T. Tantt, W. Huang, K. W. Chan, K. Y. Tan, F. E. Hudson, K. M. Itoh, A. Morello, A. Laucht, M. Pioro-Ladrière, A. Saraiva, and A. S. Dzurak, *Nat. Commun.* **11**, 797 (2020).
- [16] D. D. Awschalom, R. Hanson, J. Wrachtrup, and B. B. Zhou, *Nat. Photonics* **12**, 516 (2018).
- [17] M. Atatüre, D. Englund, N. Vamivakas, S. Y. Lee, and J. Wrachtrup, *Nat. Rev. Mater.* **3**, 38 (2018).
- [18] Y. Romach, C. Müller, T. Unden, L. J. Rogers, T. Isoda, K. M. Itoh, M. Markham, A. Stacey, J. Meijer, S. Pezzagna, B. Naydenov, L. P. McGuinness, N. Bar-Gill, and F. Jelezko, *Phys. Rev. Lett.* **114**, 017601 (2015).
- [19] H. S. Knowles, D. M. Kara, and M. Atatüre, *Nat. Mater.* **13**, 21 (2014).
- [20] M. Warner, S. Din, I. S. Tupitsyn, G. W. Morley, A. M. Stoneham, J. A. Gardener, Z. Wu, A. J. Fisher, S. Heutz, C. W. M. Kay, and G. Aeppli, *Nature (London)* **503**, 504 (2013).
- [21] K. Bader, D. Dengler, S. Lenz, B. Endeward, S. D. Jiang, P. Neugebauer, and J. Van Slageren, *Nat. Commun.* **5**, 5304 (2014).
- [22] J. M. Zadrozny, J. Niklas, O. G. Poluektov, and D. E. Freedman, *ACS Cent. Sci.* **1**, 488 (2015).
- [23] M. Atzori, L. Tesi, E. Morra, M. Chiesa, L. Sorace, and R. Sessoli, *J. Am. Chem. Soc.* **138**, 2154 (2016).
- [24] L. C. Camargo, M. Briganti, F. S. Santana, D. Stingen, R. R. Ribeiro, G. G. Nunes, J. F. Soares, E. Salvadori, M. Chiesa, S. Benci, R. Torre, L. Sorace, F. Totti, and R. Sessoli, *Angew. Chem.* **133**, 2620 (2021).
- [25] G. Balasubramanian, P. Neumann, D. Twitchen, M. Markham, R. Kolesov, N. Mizuochi, J. Isoya, J. Achard, J. Beck, J. Tissler,

- V. Jacques, P. R. Hemmer, F. Jelezko, and J. Wrachtrup, *Nat. Mater.* **8**, 383 (2009).
- [26] A. M. Tyryshkin, S. Tojo, J. J. Morton, H. Riemann, N. V. Abrosimov, P. Becker, H. J. Pohl, T. Schenkel, M. L. Thewalt, K. M. Itoh, and S. A. Lyon, *Nat. Mater.* **11**, 143 (2012).
- [27] N. Bar-Gill, L. M. Pham, A. Jarmola, D. Budker, and R. L. Walsworth, *Nat. Commun.* **4**, 1743 (2013).
- [28] M. Veldhorst, J. C. Hwang, C. H. Yang, A. W. Leenstra, B. De Ronde, J. P. Dehollain, J. T. Muhonen, F. E. Hudson, K. M. Itoh, A. Morello, and A. S. Dzurak, *Nat. Nanotechnol.* **9**, 981 (2014).
- [29] G. Wolfowicz, A. M. Tyryshkin, R. E. George, H. Riemann, N. V. Abrosimov, P. Becker, H. J. Pohl, M. L. Thewalt, S. A. Lyon, and J. J. Morton, *Nat. Nanotechnol.* **8**, 561 (2013).
- [30] M. Shiddiq, D. Komijani, Y. Duan, A. Gaita-Ariño, E. Coronado, and S. Hill, *Nature (London)* **531**, 348 (2016).
- [31] J. M. Zadrozny, A. T. Gallagher, T. D. Harris, and D. E. Freedman, *J. Am. Chem. Soc.* **139**, 7089 (2017).
- [32] S. Giménez-Santamarina, S. Cardona-Serra, J. M. Clemente-Juan, A. Gaita-Ariño, and E. Coronado, *Chem. Sci.* **11**, 10718 (2020).
- [33] E. H. Lieb, *Phys. Rev. Lett.* **62**, 1201 (1989).
- [34] Y. G. Tullimilli, W. Zeng, X. Lu, and J. Wu, *Chem. Commun.* **54**, 2186 (2018).
- [35] Y. Ni, T. Y. Gopalakrishna, H. Phan, T. S. Heng, S. Wu, Y. Han, J. Ding, and J. Wu, *Angew. Chem., Int. Ed.* **57**, 9697 (2018).
- [36] C. Liu, M. E. Sandoval-Salinas, Y. Hong, T. Y. Gopalakrishna, H. Phan, N. Aratani, T. S. Heng, J. Ding, H. Yamada, D. Kim, D. Casanova, and J. Wu, *Chem* **4**, 1586 (2018).
- [37] A. Schweiger and G. Jeschke, *Principles of Pulse Electron Paramagnetic Resonance* (Oxford University Press, Oxford, 2001).
- [38] W. Yang, W. L. Ma, and R. B. Liu, *Rep. Prog. Phys.* **80**, 016001 (2017).
- [39] W. M. Witzel, K. Young, and S. Das Sarma, *Phys. Rev. B* **90**, 115431 (2014).
- [40] P. Szańkowski, G. Ramon, J. Krzywda, D. Kwiatkowski, and Cywiński, *J. Phys.: Condens. Matter* **29**, 333001 (2017).
- [41] L. Viola and S. Lloyd, *Phys. Rev. A* **58**, 2733 (1998).
- [42] E. L. Hahn, *Phys. Rev.* **80**, 580 (1950).
- [43] H. Y. Carr and E. M. Purcell, *Phys. Rev.* **94**, 630 (1954).
- [44] S. Meiboom and D. Gill, *Rev. Sci. Instrum.* **29**, 688 (1958).
- [45] A. A. Maudsley, *J. Magn. Reson. (1969-1992)* **69**, 488 (1986).
- [46] T. Gullion, D. B. Baker, and M. S. Conradi, *J. Magn. Reson. (1969-1992)* **89**, 479 (1990).
- [47] G. S. Uhrig, *Phys. Rev. Lett.* **98**, 100504 (2007).
- [48] W. Yang and R. B. Liu, *Phys. Rev. Lett.* **101**, 180403 (2008).
- [49] K. Khodjasteh and D. A. Lidar, *Phys. Rev. Lett.* **95**, 180501 (2005).
- [50] N. Timoney, I. Baumgart, M. Johanning, A. F. Varón, M. B. Plenio, A. Retzker, and C. Wunderlich, *Nature (London)* **476**, 185 (2011).
- [51] G. T. Genov, N. Aharon, F. Jelezko, and A. Retzker, *Quantum Sci. Technol.* **4**, 035010 (2019).
- [52] G. de Lange, Z. H. Wang, D. Riste, V. V. Dobrovitski, and R. Hanson, *Science* **330**, 60 (2010).
- [53] N. Bar-Gill, L. M. Pham, C. Belthangady, D. Le Sage, P. Cappellaro, J. R. Maze, M. D. Lukin, A. Yacoby, and R. Walsworth, *Nat. Commun.* **3**, 858 (2012).
- [54] M. J. Biercuk, H. Uys, A. P. VanDevender, N. Shiga, W. M. Itano, and J. J. Bollinger, *Nature (London)* **458**, 996 (2009).
- [55] H. Bluhm, S. Foletti, I. Neder, M. Rudner, D. Mahalu, V. Umansky, and A. Yacoby, *Nat. Phys.* **7**, 109 (2011).
- [56] G. S. Uhrig, *New J. Phys.* **10**, 083024 (2008).
- [57] G. Mitrikas, E. K. Efthimiadou, and G. Kordas, *Phys. Chem. Chem. Phys.* **16**, 2378 (2014).
- [58] F. Lombardi, W. K. Myers, J. Ma, J. Liu, X. Feng, and L. Bogani, *Phys. Rev. B* **101**, 094406 (2020).
- [59] S. S. Eaton and G. R. Eaton, in *Distance Measurements in Biological Systems by EPR*, edited by L. J. Berliner, S. S. Eaton, and G. R. Eaton, Biological Magnetic Resonance (Springer, 2006), Vol. 19.
- [60] F. Fajarsa, B. Geil, H. Sillescu, and G. Fleischer, *Z. Phys. B* **88**, 195 (1992).
- [61] M. D. Ediger, C. A. Angell, and S. R. Nagel, *J. Phys. Chem.* **100**, 13200 (1996).
- [62] A. E. Dementyev, D. Li, K. MacLean, and S. E. Barrett, *Phys. Rev. B* **68**, 153302 (2003).
- [63] D. Li, A. E. Dementyev, Y. Dong, R. G. Ramos, and S. E. Barrett, *Phys. Rev. Lett.* **98**, 190401 (2007).
- [64] D. Li, Y. Dong, R. G. Ramos, J. D. Murray, K. MacLean, A. E. Dementyev, and S. E. Barrett, *Phys. Rev. B* **77**, 214306 (2008).
- [65] V. V. Kurshev and A. M. Raitsimring, *J. Magn. Reson. (1969-1992)* **88**, 126 (1990).
- [66] J. Du, X. Rong, N. Zhao, Y. Wang, J. Yang, and R. B. Liu, *Nature (London)* **461**, 1265 (2009).
- [67] J. Soetbeer, M. Hülsmann, A. Godt, Y. Polyhach, and G. Jeschke, *Phys. Chem. Chem. Phys.* **20**, 1615 (2018).
- [68] There are limitations to the number of steps that can be performed, with each additional pulse increasing the measurement time exponentially. We determined that measurement times would be reasonable up to a 256-step phase cycling, but anything above would become cumbersome. Therefore, we established a cycled approach in which we decompose a sequence of  $n > 8$  pulses into equal blocks of three, four, or five  $\pi$  pulses, for which we applied 8-step, 16-step, and 32-step phase cyclings. While this is not the same as a  $2^n$ -step phase cycling, the results in Figs. 5(b) and 5(c) for  $n > 8$  are consistent with what is observed for the full-phase cycling.
- [69] C. A. Ryan, J. S. Hodges, and D. G. Cory, *Phys. Rev. Lett.* **105**, 200402 (2010).
- [70] P. P. Borbat, E. R. Georgieva, and J. H. Freed, *J. Phys. Chem. Lett.* **4**, 170 (2013).
- [71] J. Medford, L. Cywiński, C. Barthel, C. M. Marcus, M. P. Hanson, and A. C. Gossard, *Phys. Rev. Lett.* **108**, 086802 (2012).
- [72] W. Han, R. K. Kawakami, M. Gmitra, and J. Fabian, *Nat. Nanotechnol.* **9**, 794 (2014).
- [73] W. Zhang, J. Zhang, J. Wang, F. Feng, S. Lin, L. Lou, W. Zhu, and G. Wang, *Phys. Rev. B* **96**, 235443 (2017).